ASTRONOMY & ASTROPHYSICS
SUPPLEMENT SERIES

Astron. Astrophys. Suppl. Ser. **130**, 551–560 (1998)

Beam distortion effects on anisotropy measurements of the cosmic microwave background

C. Burigana[1], D. Maino[2], N. Mandolesi[1], E. Pierpaoli[2], M. Bersanelli[3], L. Danese[2], and M.R. Attolini[1]

[1] Istituto TeSRE, Consiglio Nazionale delle Ricerche, Via Gobetti 101, 40129 Bologna, Italy
[2] SISSA, International School for Advanced Studies, Via Beirut 2-4, 34014 Trieste, Italy
[3] IFCTR, Consiglio Nazionale delle Ricerche, Via Bassini 15, 20133 Milano, Italy

Received November 7; accepted December 18, 1997

Abstract. High resolution observations of CMB anisotropy requires the use of feed arrays at the focus of an optical system. Beam responses are typically not symmetric for array elements de-centred from the telescope focus, whereas theoretical predictions and standard deconvolution methods generally assume pure symmetric beams. For estimating the effect of main beam asymmetry on temperature fluctuations measurements we have generated high resolution sky maps by using standard spherical harmonics expansion for the CMB fluctuations and by extrapolating available full sky maps to predict Galaxy emission at frequencies and angular scales appropriate to future space missions, like Planck and MAP. We have then convolved simulated maps of the microwave sky with asymmetric beams by adopting the Planck configuration and scanning strategy. We find that the typical difference between temperature measurements performed by symmetric and asymmetric beams is of few μK and that it is an increasing function of the beam eccentricity and FWHM. Although this effect is not very large, it is of order of the ultimate sensitivity of the next generation of experiments, and must be reduced by optimizing the feedhorns locations on the focal plane.

Key words: cosmology: cosmic microwave background — diffuse radiation — methods: data analysis — telescopes

1. Introduction

Future space missions, like Planck and MAP, represent a powerful opportunity for Cosmology through the imaging of the cosmic microwave background (CMB) with great sensitivity and angular resolution. The instrument design for these space missions, as well as for a number other on-going sub-orbital CMB projects (e.g. BEAST, Boomerang, TopHat), calls for multi-frequency focal plane arrays placed at the focus of off-axis optical systems, in order to achieve proper angular resolution, sensitivity, and spectral coverage. As a consequence, not all the feedhorns can be located very close to the centre of the focal plane, where optical distortions are minimum. Optical distortions make the main beam response somewhat different from a pure gaussian, centrally symmetric shape. In addition, sidelobe effects may become more prominent and affect the measurements, an effect that will be studied in a forthcoming work. Main beam distortions may introduce two kinds of effects on anisotropy measurements: a degradation of the effective angular resolution achievable by a given experiment and a sensitivity degradation in the evaluation of the temperature anisotropy in any resolution element. Roughly speaking, these two effects can be seen as orthogonal one each other in the space $\theta - \Delta T$ of angular scales and temperature anisotropy or equivalently in the space of $l - C_l$ of multipoles and angular power spectrum. The former shifts toward low multipoles the effective angular sensitivity of an experiment (see White 1997 and Mandolesi et al. 1997, 1998 for a discussion of this effect for Planck surveyor mission); the latter increases the final error in the determination of angular power spectrum. Here we focus on the relevance in anisotropy measurements of this second effect generated by main beam distortions.

The generation of high resolution full sky maps, consistent with the COBE-DMR normalization of the CMB anisotropies and based on reasonable angular and frequency extrapolations of the available galactic emission maps, is a basic step for simulating the mission performance.

In Sect. 2 we outlined the basic framework for generating full sky maps including CMB anisotropy and Galaxy diffuse emission. In Sect. 3 we present the method adopted to convolve the simulated map with a beam of general shape, taking into account the mission observational

Send offprint requests to: burigana@tesre.bo.cnr.it

strategy (we refer here to the standard Planck scanning strategy, but the method can be applied to other observational schemes). The main results of our beam tests and empirical formulas that accurately quantify the effect of beam distortion on temperature measurements as functions of the relevant parameters are presented in Sect. 4. In Sect. 5 we discuss the effect of main beam distortions in presence of a relevant galactic signal. Finally, in Sect. 6 we draw out the main implications of this analysis focussing on their impact for the optimization of the feedhorns locations on the Planck focal plane.

2. Generation of simulated maps

In this section we briefly present the basic issues for generating high resolution full sky maps which include CMB fluctuations and the galactic emission.

2.1. CMB fluctuation maps

The CMB anisotropy is usually written as (Bond & Efstathiou 1987; White et al. 1994):

$$\frac{\Delta T(\vartheta,\phi)}{T} = \sum_{l=0}^{\infty} \sum_{m=-l}^{l} a_{lm}\, Y_{lm}(\vartheta,\phi) \tag{1}$$

where $Y_{l,m}(\vartheta,\phi)$ are the usual spherical harmonics (Press et al. 1987). They can be expressed as a product of the Legendre polynomials, P_l^m, where is all the dependence on colatitude ϑ, and an exponential factor that contains the dependence upon longitude ϕ. Provided that the anisotropies are a gaussian random field, the a_{lm} coefficients are randomly distributed variables with zero mean and variance $C_l =< |a_{lm}|^2 >$. The coefficients C_l define the angular power spectrum obtained from a given cosmological model. The Legendre polynomials can be evaluated by the standard recurrence relations (e.g. Press et al. 1987). These relations in some cases are inadequate to evaluate the P_l^m, expecially at high values of l, and we have worked with a slightly modified set of polynomials, p_l^m, and the corresponding recurrence relations, related to the Legendre polynomials by:

$$p_l^m(\mu) = \sqrt{\frac{(l-m)!}{(l+m)!}} P_l^m(\mu)\,, \tag{2}$$

where $\mu = \cos(\vartheta)$. With this notation, from the reality of the temperature anisotropies we have that the temperature fluctuations can be expressed as:

$$\begin{aligned}\frac{\Delta T(\vartheta,\phi)}{T} = & \sum_{l=2}^{l_{\max}} \sqrt{\frac{2l+1}{4\pi}} p_l^0(\mu) \Re e(a_{l0}) \\ & + \sum_{m=1}^{l_{\max}} \sum_{l=\mathrm{Max}\{2,m\}}^{l_{\max}} 2\sqrt{\frac{2l+1}{4\pi}} p_l^m(\mu) [\Re e(a_{lm}) \\ & \times \cos(m\phi) - \Im m(a_{lm}) \sin(m\phi)]. \end{aligned} \tag{3}$$

We have choosen to neglect here the cosmological dipole term, $l = 1$, which is dominated by the Doppler effect due to the relative motion of the earth relative to the CMB.

In Eq. (3) only the polynomials p_l^m depend on ϑ, while all the dependence on ϕ is in the square bracket part. This particular feature makes the choice of the pixelisation (i.e. the set of $\{\vartheta_i, \phi_j\}$ where to calculate $\Delta T/T$) a crucial parameter for the computational cost of the simulation. The "standard" COBE-cube pixelisation satisfies two simple symmetry properties: 1) if $\vartheta_k \in \{\vartheta_i\}$, then also $-\vartheta_k \in \{\vartheta_i\}$; 2) if $\phi_k \in \{\phi_j\}$ then also $(\phi_k + \pi) \in \{\phi_j\}$. It allows to divide by four the computational time because the temperature anisotropy can be computed in four points of the sky at the same time. It offers the advantage of good equal-area conditions, hierarchic and also Galaxy maps and software are presently available for that pixelisation scheme (see Gorski (1997) for an improved scheme which also includes the recepies of Muciaccia et al. (1997) that strongly reduce the computational load).

From a simulated map we can compute the usual correlation function $C(\theta)_{\mathrm{map}}$ (Peebles 1972). Directly from the a_{lm}, and the corresponding $C_{l,\mathrm{map}}$ used for generating a given map we can have the correlation function $C(\theta)_{a_{lm}}$. We have generated maps at angular resolutions (i.e. typical pixel dimensions) of about $19'$, $10'$, $5'$, corresponding respectively to COBE-cube resolutions R equal to 9, 10 and 11 and with l up to 1200 and we have verified the goodness of the maps obtained with our code by comparing the correlation functions obtained from the two above methods, in order to avoid the ambiguity due to the cosmic variance. In addition we have checked that the average of the correlation functions obtained by few tens of maps tends to that derived from the theoretical prescription for the C_l.

2.2. Galactic emission

In the spectral range of interest here, the galactic emission is due to three different physical mechanisms: synchrotron emission from cosmic ray electrons accelerated by galactic magnetic fields, free-free or thermal bremsstrahlung emission and dust emission.

To first approximation, both synchrotron and free-free spectral shape can be described, in terms of antenna temperature, by simple power laws, $T(\nu) \propto \nu^{-\alpha}$, with spectral indeces $\alpha_{\mathrm{syn}} = 2.8 - 3.1$ and $\alpha_{\mathrm{ff}} = 2.1$ respectively. While free-free emission is a well known mechanism and α_{ff} has relatively small uncertaintes, the synchrotron emission is still rather unknown and, as derived from the theory, a steepening of the spectral index is expected at higher frequencies (Lawson et al. 1987; Banday & Wolfendale 1990, 1991). It is also expected a spatial variation of α_{syn} due to its dependence upon electrons energy density and galactic magnetic field (Lawson et al. 1987; Banday & Wolfendale 1990, 1991; Kogut et al. 1996; Platania et al. 1998).

Dust emission spectral shape can be described by a simple modified blackbody law $I_\nu \propto \nu^\alpha B_\nu(T)$ where α is the emissivity and $B_\nu(T)$ is the brightness of a blackbody of temperature T. Recent works, based upon COBE-DMR and $DIRBE$ data (Kogut et al. 1996), give values of $\alpha \sim 1.8-2$ and $T \sim 18$ K; a recent analysis of $FIRAS$ maps (Burigana & Popa 1998) supports a model with two dust temperatures (Wright et al. 1991; Brandt et al. 1994).

In order to build up a realistic model of galactic emission we have to know both spatial and spectral behaviour of the three emission mechanisms. Useful information can be obtained from measurements in those spectral regions where only one of these emission mechanisms is dominant.

This is possible only for synchrotron emission (at very low frequencies) and for dust emission (at very high frequencies), while free-free emission does not dominate in any frequency range. Our model does not yet include free-free emission in our Galaxy but this does not significantly affect the results of our beam tests. For our simulation of the synchrotron emission we took a spectral index (between 2.8 and 3.1) that is constant on the whole sky, i.e. we did not allow any spatial variation in $\alpha_{\rm syn}$. Also we are able to select different dust models; here we used the two dust temperature model of Brandt et al. (1994).

The simulated maps are based upon two full-sky maps: the map of Haslam et al. (1982) at 408 MHz and $DIRBE$ map at 240 μm. Both maps have nearly the same angular resolution ($\theta \sim 0.85^\circ$ and 0.6° respectively) which is clearly not sufficient to simulate directly the Planck observations ($\theta \lesssim 30'$).

Studies on the spatial distribution and angular power spectrum of galactic emission (Gautier et al. 1992; Kogut et al. 1996) show that dust and at least one component of the free-free follow a power law $C_l \propto l^{-\beta}$, with $\beta = 3$. For synchrotron emission the situation is still unclear, the index probably ranging from 2 to 3, although a recent study (Lasenby 1997) indicates a value closer to 2 (our analysis of Haslam map tends to confirm this spectral shape).

In order to match the proper Planck resolution we can extend in power the present galactic maps. A complete, self-consistent approach will require their inversion in order to obtain the coefficients a_{lm} in the range of l, m covered by the maps resolution. Then, one may extrapolate the coefficients a_{lm} at large values of l (and $|m|$), possibly according to some physical, frequency dependent model for Galaxy fluctuations at small angular scales. This analysis is out of the aim of the present work.

In order to generate high resolution galactic maps we adopted here a simple euristic approach which is only a first guess but which is neverthless a reasonable choice. Firstly, we increase the original angular resolution (of about $19'$) of a given map (Haslam and DIRBE) in an artificial way, by dividing each pixel of this map in smaller pixels (of about $5'$) with the same temperature of the larger pixel that contains them. We want now the temperature field oscillates within this scale. We then calculate from the original map the RMS fluctuation on a certain angular scale (in our case we took 2.6°). Then we built a suitable number of squared regions of about $20^\circ \times 20^\circ$ with an "extended" angular power spectrum $C_l \propto l^{-\beta}$ (we have considered the cases of $\beta = 2$ or 3) with a resolution of about $5'$ (corresponding to the COBE-cube pixelisation at $R = 11$) and considering the multipoles from l corresponding to a scale 2.6° up to $l = 2000$. We randomly "covered" the whole RMS sky with these patches by locally rescaling them requiring that the RMS in the different regions of 2.6° size in the extended map has to be the same found from the original map; this determines the normalization of the "extended" angular power spectrum. Finally we add the "extended" RMS sky to the above artificial "extended" sky, that were uniform on scales of $19'$. In this way we add fluctuations on smaller angular scales starting from what the fluctuations really are on larger angular scales. We have checked that this extended map, degraded at a COBE-cube resolution 9, presents pixels temperatures that differ from those of the original map for only few percent, substantially confirming the stability of the method.

Finally, the signal in these maps is scaled in frequency according to the spectral shapes described above in order to match the Planck frequencies. In particular we built two maps of the galactic emission at 30 and 100 GHz (with both synchrotron and dust emission) that we used for the present beam tests.

3. Convolution of the simulated map with the beam response

We have written a code that simulates the basic properties of Planck observations in order to study the effect of beam distortions on the measured sky temperatures. The sky is simulated adding the CMB and galactic components as described in Sect. 2.

Different feedhorns must be located on different parts of the focal plane. The magnitude and the kind of beam distortion depend on several parameters: the beam FWHM, the observational frequency, the telescope optical scheme and the beam location with respect to the optical axis. Optical simulations (Nielsen & Pontoppidan 1996) show that the main expected distortion in the off-axis beams has a roughly elliptical shape, with more complex asymmetries in the sidelobe structure. We have assumed here that the beam is located along the optical axis, but that it can have an elliptical shape, i.e. the curves of equal response are ellipses. This assumption has to be considered here as a simple work-hypothesis, not far from the truth, useful for deriving a general description of the magnitude of the main beam distortion effect as a function of few basic parameters (see Sect. 4). More detailed studies are in progress for taking into account realistic beam shapes for the Planck optic (Mandolesi et al. 1997, 1998).

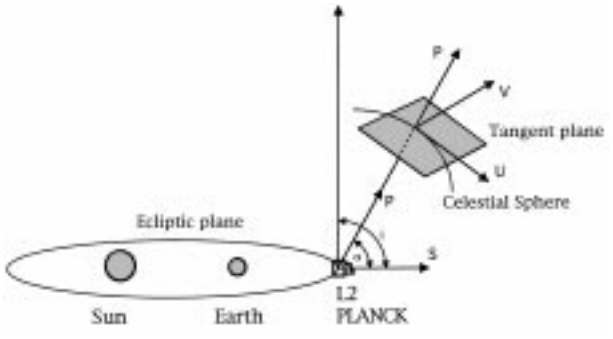

Fig. 1. Schematic representation of the observational geometry

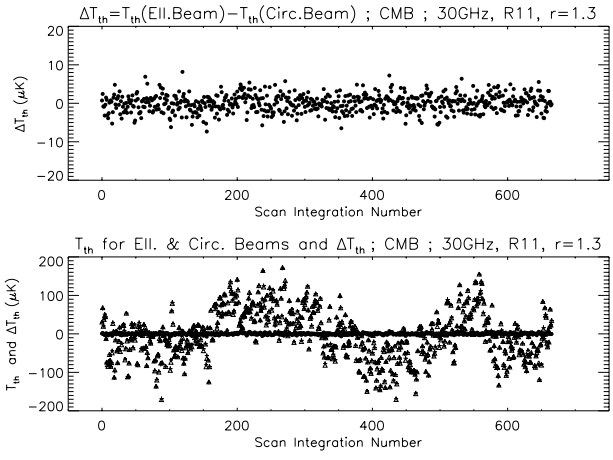

Fig. 2. Top panel: difference between the thermodynamic temperature observed by asymmetric and symmetric beams for a typical scan circle as function of the scan integration number along the circle. Bottom panel: thermodynamic temperature observed by asymmetric (triangles) and symmetric (crosses) beams and differences (circles) between the two measurements for the same scan circle. The figure refers to the test 2 in Table 1

Figure 1 shows the schematic representation of the observational geometry. Let be i the angle between a unit vector, $\boldsymbol{s}$, along the satellite spin axis outward the Sun direction and the normal to the ecliptic plane and $\boldsymbol{p}$ the unit vector of the direction of the optical axis of the telescope, at an angle α from the spin axis ($i = 90^\circ$ and $\alpha = 70^\circ$ for the Phase A study, Bersanelli et al. 1996). We choose two coordinates x and y on the plane tangent to the celestial sphere in the optical axis direction, with unit vector $\boldsymbol{u}$ and $\boldsymbol{v}$ respectively; we choose the x axis according to the condition that the unit vector $\boldsymbol{u}$ points always toward the satellite spin axis; indeed, for the standard Planck observational strategy, this condition is preserved as the telescope scans different sky regions. With this choice of reference frame, we have that $\boldsymbol{v} = \boldsymbol{p}\wedge\boldsymbol{s}/|\boldsymbol{p}\wedge\boldsymbol{s}|$ and $\boldsymbol{u} = \boldsymbol{v}\wedge\boldsymbol{p}/|\boldsymbol{v}\wedge\boldsymbol{p}|$ (here $\wedge$ indicates the vector product). In general the coordinates (x_0, y_0) of the beam centre will be identified by two angles (e.g. the colatitude and the longitude) in the $\boldsymbol{u}, \boldsymbol{v}, \boldsymbol{p}$ reference frame. Then, the beam (elliptical) response in a given point (x, y) is given by:

$$K(x,y) = \exp\left[-\frac{1}{2}[((x-x_0)/\sigma_x)^2 + ((y-y_0)/\sigma_y)^2]\right] . \quad (4)$$

In practice, for the present study we can take $x_0 = y_0 = 0$.

The ratio $r = \max(\sigma_x, \sigma_y)/\min(\sigma_x, \sigma_y)$ between major and minor axis of the ellipses of constant response quantifies the amount of beam distortion respect to the case of a pure symmetric beam with $\sigma'_x = \sigma'_y = \sigma' = \sqrt{\sigma_x \sigma_y}$ (we have choosen the major axis along the x axis, but we have verified for a suitable number of cases that our conclusions are unchanged if the major axis is choosen along the y axis). We have convolved the simulated map with this beam response up to the level $(x/\sigma_x)^2 + (y/\sigma_y)^2 = 9$, i.e. up to the 3σ level ($\simeq -20$ dB). The integration has been performed by using a 2-dimensional gaussian quadrature with a grid of 48×48 points. We have performed the convolution under the assumption that the telescope points always at the same direction during a given integration time; this artificially simplifies the analysis, but it is useful to make the study independent of the scanning strategy and related only to the optical properties of the instrument. We will study the effect introduced by the telescope motion in a future work (see Sect. 4.8). The sky map, obtained by using the COBE-cube pixelisation, has been interpolated in a standard way to have the temperature values at the grid points. For maps at resolution 11 (9) we have about 50 (3) pixels within the FWHM ($\simeq 30'$) at 30 GHz and 6 (less than 1) at 100 GHz (FWHM $\simeq 12'$); then the true accuracy of the integration depends not only on the adopted integration technique but on the map resolution too. For this reason the use of high resolution maps and a careful comparison between beam test results obtained from maps at different resolutions are recommended.

In order to quantify how the beam distortion affects the anisotropy measurements, we use a simple estimator: the rms of the difference between the temperature observed by an elliptical beam and by a symmetric one. We express it here in terms of thermodynamic temperature, which does not depend on the observational frequency; the present results can be translated in terms of antenna temperature with the relation $\mathrm{rms_A} = \mathrm{rms_{th}} x^2 \exp(x)/[\exp(x) - 1]^2$ where $x = h\nu/kT_0$, where $T_0 = 2.726$ K is the CMB thermodynamic temperature ($\mathrm{rms_A} \simeq \mathrm{rms_{th}}$ at 30 GHz, whereas $\mathrm{rms_A} \simeq 0.777\ \mathrm{rms_{th}}$ at 100 GHz).

4. Results of beam tests

For sake of clarity, we have first performed our simulations neglecting the galactic emission in order to obtain general results holding for low foreground regions. A flat CDM model with $H_0 = 50$ km/s/Mpc and a baryon density in terms of critical density $\Omega_\mathrm{b} = 0.05$, with a 24% of mass in Helium, has been adopted for the present tests, but some other models have been considered for comparison

Table 1. $\mathrm{rms_{th}}$ value of $(T_{\mathrm{ell}} - T_{\mathrm{circ}})$ for the cases presented in Sect. 4.1

Test−CDM	ν(GHz)	FWHM	d	R	r	$\mathrm{rms_{th}}(\mu\mathrm{K})$	$\Delta\mathrm{rms_{th}}(\mu\mathrm{K})$
1)	30	$30'$	$4.86'$	11	1.1	0.834	0.16
2)	30	$30'$	$4.86'$	11	1.3	2.27	0.16
3)	30	$30'$	$4.86'$	11	1.8	5.09	0.16
4)	100	$12'$	$4.86'$	11	1.1	0.506	0.10
5)	100	$12'$	$4.86'$	11	1.3	1.38	0.10
6)	100	$12'$	$4.86'$	11	1.8	3.19	0.10
7)	30	$30'$	$19.4'$	9	1.3	1.39	

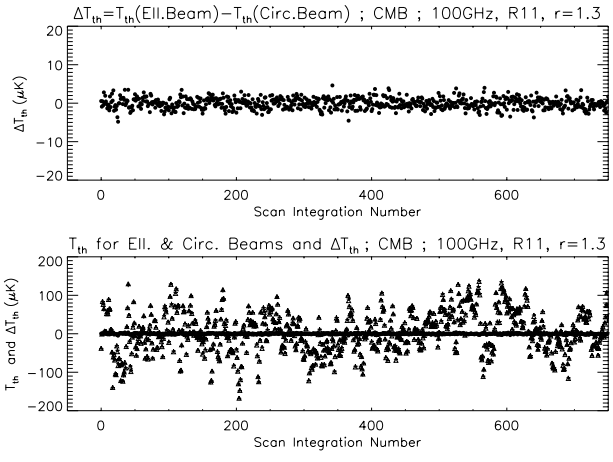

Fig. 3. The same as Fig. 2 but at 100 GHz (see test 5 in Table 1)

(see Sect. 4.7). For the standard Planck scanning strategy, a test on a given scan circle consists of about 680 integrations at 30 GHz and of about 1700 integrations at 100 GHz. We can estimate the numerical error introduced by interpolation and integration techniques by comparing for few cases the results obtained by using an integration grid of 48×48 points with those obtained with a grid of 96×96 points (see Col. 8 of Table 1).

4.1. Results from high resolution maps

We have firstly performed our tests using maps at a resolution of about $5'$ (COBE-cube resolution 11). Figures 2 and 3 show our results for a typical test at 30 GHz and at 100 GHz respectively. Even in correspondence of the largest temperature variations induced by CMB quadrupole large scale waves, the temperature differences remain practically equal to those obtained in other sky regions (see the bottom panels of Figs. 2 and 3).

Typical results obtained by using maps at COBE-cube resolution $R = 11$ are tabulated in Table 1 (tests 1–6) in terms of $\mathrm{rms_{th}}$ for different beam FWHM's and distortion parameters r. Column 8 in Table 1 gives the numerical error, $\Delta\mathrm{rms_{th}}$, in the determination of $\mathrm{rms_{th}}$ derived from the comparison of results obtained for a typical scan circle with a symmetric beam by using different integration grids (of course the reported value of $\Delta\mathrm{rms_{th}}$ is $\sqrt{2}$ times that derived from this test).

These results may be qualitatively interpreted from a geometrical point of view: the contribution of the different parts of the sky observed by beams with different shapes becomes more important and produces a growing effect as the FWHM and/or r increases (Burigana et al. 1997).

On the other hand we may expect that these results depend in part on the resolution of the maps used for the test. Indeed the use of maps at lower resolution tends to smear out the differences of temperature between different pixels and we expect that the value of $\mathrm{rms_{th}}$ may decrease by passing from higher to lower resolution maps, as confirmed by the results of the test 7 in Table 1, performed by using the same map at 30 GHz of the above tests but degraded at a lower resolution (see Sect. 4.4).

4.2. Searching for an analytical description of beam distortion effect

The results of the previous section indicate that $\mathrm{rms_{th}}$ mainly depends on three quantities: the beam distortion parameter, r, the beam FWHM$'$, where the suffix "prime" indicates that it is expressed in arcminutes, and the map resolution, R, or equivalently the typical pixel dimension, d. A simple expression for the beam distortion effect as function of these parameters can be useful for many purposes. We will search here for a formula based on the assumption of separability of the variables, i.e. of the kind:

$$\mathrm{rms_{th}} = \mathrm{const} \cdot f[\mathrm{FWHM}'; (d/\mathrm{FWHM}), r] \cdot g[(d/\mathrm{FWHM}); \mathrm{FWHM}', r] \cdot h[r; (d/\mathrm{FWHM}), \mathrm{FWHM}'] \,, \quad (5)$$

where the function f, g, h depends only on their first argument, i.e. the quantities after ";" are considered constant. This simple work-hypothesis allow us to obtain an analytical description of the main beam distortion effect with a relatively small number of simulations. We have later verified that it is accurate enough for the present purposes (see Sect. 4.6). In the following sections we present numerical tests that allow to derive simple but quite accurate representations of these functions.

Table 2. $\mathrm{rms_{th}}$ value of $(T_{\rm ell} - T_{\rm circ})$ for the cases presented in Sects. 4.3 and 4.4

Test−CDM	ν(GHz)	FWHM	d	R	r	$\mathrm{rms_{th}}(\mu\mathrm{K})$
8)	30	$9'$	$4.86'$	11	1.3	0.987
9)	30	$18'$	$9.72'$	10	1.3	1.39
10)	30	$36'$	$19.4'$	9	1.3	1.55
11)	30	$72'$	$38.8'$	8	1.3	1.43
12)	30	$18'$	$4.86'$	11	1.3	1.84
13)	30	$18'$	$9.72'$	10	1.3	1.39
14)	30	$18'$	$19.4'$	9	1.3	0.818

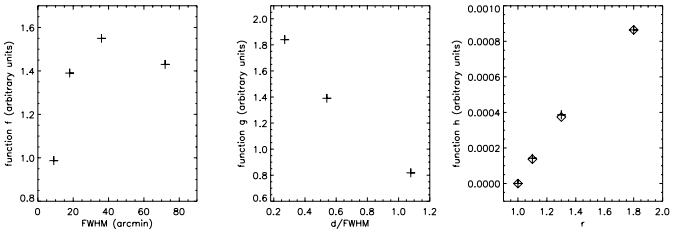

Fig. 4. From the left to the right: the function f versus the beam FWHM as derived from the tests 8–11; the function g versus d/FWHM as derived from the tests 12–14; the function h versus r as derived form the tests 1–6 (crosses: tests at 30 GHz; diamonds: tests at 100 GHz; see Sect. 4.5)

4.3. Dependence on the beam FWHM

For understanding the dependence of $\mathrm{rms_{th}}$ on the beam FWHM we have performed four tests by keeping constant the ratio, d/FWHM, between the typical pixel dimension and the beam size, and the beam distortion parameter r. We have considered a case with a beam size (FWHM $= 72'$) somewhat larger than those of Planck LFI radiometers in order to give results holding also for observations performed with smaller telescopes. The corresponding results are tabulated in Table 2 (tests 8–11). They can be well described by a function f (see left panel of Fig. 4):

$$f[\mathrm{FWHM}'; (d/\mathrm{FWHM}), r] \propto - \mathrm{FWHM}'^2 + 96.0\,\mathrm{FWHM}' + 1800\,. \quad (6)$$

We note that this function presents a maximum at FWHM $\sim 48'$; indeed (see tests 10 and 11 in Table 2) for FWHM of about 1° the beam distortion effect is smaller than for example for FWHM of about 0.5°; this fact can be produced by the smearing out of the effect related to the different contribution of the parts of the sky observed by beams with different distortion parameters, when the beam size is large enough.

4.4. Dependence on the map resolution

For understanding the dependence of $\mathrm{rms_{th}}$ on the ratio d/FWHM we have carried out three tests by keeping constant the beam size and the beam distortion parameter r. We have choosen a value FWHM $= 18'$ which is intermediate between those relevant for Planck LFI radiometers. The corresponding results are tabulated in Table 2 (tests 12–14). They can be well described by a function g (see middle panel of Fig. 4):

$$g[(d/\mathrm{FWHM}); \mathrm{FWHM}', r] \propto -(d/\mathrm{FWHM}) + 1.72\,. \quad (7)$$

4.5. Dependence on the beam distortion parameter

The results of the tests 1–6 in Table 1 cannot be directly used to estimate the dependence of the beam distortion effect on the beam distortion parameter r, being based on maps with different ratios d/FWHM and different FWHM. On the other hand from Eqs. (6) and (7) we know how these two parameters may affect the test. Then we fit the values of $\mathrm{rms_{th}}$ of the tests 1–6 in Table 1 divided by the functions f and g. By including the obvious condition of null distortion effect in the case $r = 1$, for the function h we obtain the simple expression (see right panel of Fig. 4):

$$h[r; (d/\mathrm{FWHM}), \mathrm{FWHM}'] \propto -(r-1)^2 + 2.26(r-1)\,. \quad (8)$$

4.6. Normalization of the analytical approximation

Given the function f, g, h we can easily find the normalization constant of the Eq. (5) by exploiting the results of Tables 1 and 2 together. Finally we have the formula:

$$\begin{aligned}\mathrm{rms_{th}} \simeq\ & 6.43\ 10^{-4}\,\mu\mathrm{K}[-(r-1)^2 + 2.26(r-1)] \\ & \times\ [-(d/\mathrm{FWHM}) + 1.72] \\ & \times\ [-\mathrm{FWHM}'^2 + 96.0\,\mathrm{FWHM}' + 1800]. \end{aligned} \quad (9)$$

This approximation works quite well for FWHM $\lesssim 1^\circ$, as we have verified by comparing it with the results of Tables 1 and 2 and a few number of other different tests. Typical errors are about 0.25 μK and always less than 0.7 μK and it works even better for $r \lesssim 1.3$ (typical errors less than 0.1 μK). We note that tests based on sky maps directly simulated at low resolution, and not obtained from degradation of high resolution maps, tend to show a somewhat larger effect (for example about 30% greater for $R = 9$). In the asymptotic case of maps at very high resolution ($d \to 0$) we can neglect the dependence on d, by setting $g = 1$, and replace the proportionality constant with $\simeq 1.11\ 10^{-3}\,\mu$K in Eq. (9).

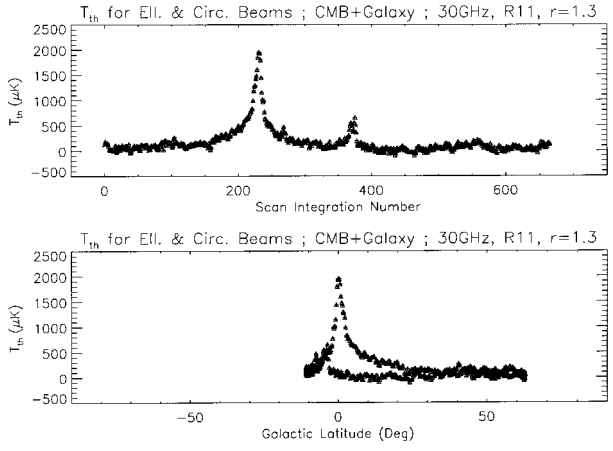

Fig. 5. Thermodynamic temperature observed by asymmetric (triangles) and symmetric (crosses) beams for a typical scan circle as function of the scan integration number along the circle (top panel) or the corresponding galactic latitude (bottom panel). The higher and lower peaks reflect the crossings with the Galactic plane near and far from the galactic centre respectively, whereas the other slow variations are essentially generated by the CMB quadrupole large scale waves. The figure refers to a test analogous to the test 2 in Table 1, but including Galaxy emission with small scales fluctuations extrapolated assuming $\beta = 2$

4.7. Check for other cosmological models

The above results are obtained by exploiting a simulated sky map in the case of pure CDM model for CMB fluctuations. We have performed other tests with different cosmological scenarios. We have considered the case of a beam with a FWHM of $18'$ and a beam distortion parameter $r = 1.3$ for two maps directly generated at resolution $R = 10$ obtained for a flat MDM model ($\Omega_{\rm Hot} = 0.3$, $\Omega_{\rm Cold=0.65}$, $\Omega_{\rm b} = 0.05$, $H_0 = 50$ km/s/Mps) and for a flat ΛCDM model ($\Omega_\Lambda = 0.7$, $\Omega_{\rm Cold} = 0.25$, $\Omega_{\rm b} = 0.05$, $H_0 = 50$ km/s/Mps). We have $\mathrm{rms_{th}} = 1.56$ and $1.74\,\mu$K respectively, in good agreement with the results of Sect. 4.6.

4.8. Averaging over three samplings

Although the accurate study of the effect of beam distortions when the telescope rotation around the satellite spin axis is taken into account is far from the purposes of the present work, we consider here that the Planck sampling scheme assumes 3 samplings per FWHM. During this time the telescope continuously changes its pointing direction; we have carried out a simulation neglecting the telescope motion within a single sampling time, but assigning to each of the 3 samplings a different telescope direction, so roughly considering the telescope motion during the integration time. We simply compare the average of three samplings obtained by a symmetric beam with that obtained by an elliptical one. When we compute the differences between these two data streams for a typical scan on a pure CMB fluctuation map for a distortion parameter $r = 1.3$ (the case of the test 2) we obtain a $\mathrm{rms_{th}}$ value of $1.85\,\mu$K, just a little lower than that found for the test 2. This test indicates that the oversampling of the sky introduced by the telescope motion cannot be used in simple way to significantly reduce the effect of main beam distortions on anisotropy measurements, as intuitively expected from the fact that during an integration time does not change significantly the orientation of a distorted beam respect to the observed sky region.

5. The effect of Galaxy fluctuations

The results presented above hold in absence of significant Galaxy contamination. On the other hand we expect that main beam distortions may be more sensitive to the larger temperature gradients due to diffuse Galaxy emission. We have then carried out simulations for circle scans crossing the Galaxy plane in two regions near the galactic centre and far from the galactic centre to check the impact of Galaxy temperature gradients in different situations (see Fig. 5). Again we have considered two frequencies, 30 GHz, where the emission of the Galaxy and its fluctuations are significant, and 100 GHz, where they are much smaller than the CMB ones (Toffolatti et al. 1995; Danese et al. 1996), and two scaling laws, $C_l \propto l^{-2}$ and $C_l \propto l^{-3}$, to extrapolate its fluctuations at small angular scales ($\lesssim 0.5^\circ - 1^\circ$). Figure 6 (top panel) shows the difference between the temperature measured by symmetric and elliptical beams as function of the anisotropy temperature for a case corresponding to the test 2 of Table 1, but including the Galaxy contribution. The temperature differences typically increase with the signal; in this case for the whole scan circle we find $\mathrm{rms_{th}} = 2.49\,\mu$K, not significantly higher than the value found for the test 2. On the other hand, by averaging only over the points with a signal larger than $200\,\mu$K, i.e. where the galactic emission dominates, we find $\mathrm{rms_{th}} = 3.22\,\mu$K.

For the same case considered in Figs. 5 and 6, the solid line in Fig. 7 shows the value of $\mathrm{rms_{th}}$ as function of the galactic latitude when we bin the temperature differences in steps of 3.5°. The beam distortion effect does not increase significantly in the regions far from the galactic plane but it can be 2–3 times larger at galactic latitudes less than about 5°. We find essentially the same result by adopting a different scaling law, $C_l \propto l^{-3}$, for Galaxy fluctuations (dashed line). A similar effect does not appear at 100 GHz (dotted line) where the impact of Galaxy emission is negligible; we find indeed the same results found in the test 5 in Table 1. Although the difference between the temperature measured by symmetric and elliptical beams can increase by a factor 2 or 3 at 30 GHz due to the Galaxy contamination, the relative error in CMB anisotropy plus

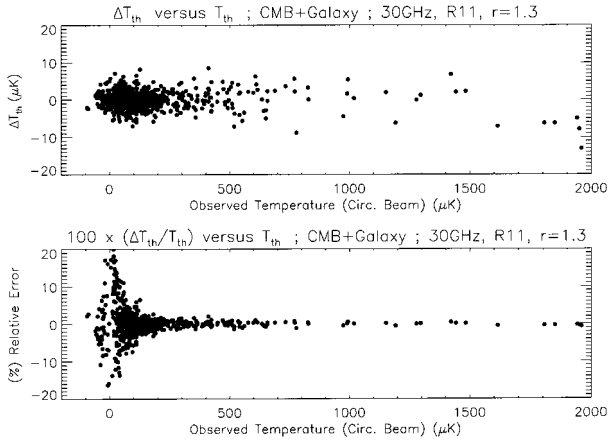

Fig. 6. Absolute (top panel) and relative (bottom panel) difference between the thermodynamic temperature observed by asymmetric and symmetric beams for the case of Fig. 5 as function of the temperature measured by the symmetric beam. The increase of the beam distortion effect at high galactic signal is evident (top panel), but the relative error remains small (bottom panel). (The high relative error at small signals is of course not relevant)

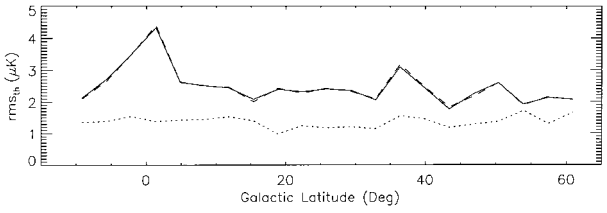

Fig. 7. Values of $\mathrm{rms_{th}}$ from the observed temperature differences between asymmetric and symmetric beams as a function of galactic latitude binned in steps of 3.5°. Different lines refer to two tests at 30 GHz with of a slope $\beta = 2$ for the Galaxy angular power spectrum (solid line) and a slope 3 (dashed line) and to a test at 100 GHz with a slope 2 (dotted lines). For all the cases we have adopted a CDM model for CMB fluctuations and a beam distortion parameter $r = 1.3$

Galaxy temperature measurements does not increase significantly where the galactic signal is high (see Fig. 6, bottom panel) and remains always less than few per cent. Then, in those sky regions where high galactic emission prevents an accurate determination of CMB fluctuations, an accurate determination of Galaxy emission in not significantly affected by main beam distortions.

6. Discussion and conclusions

In the previous section we have shown that, except for low frequency measurements in regions quite close to the galactic centre, the typical difference between the temperature measured by symmetric and distorted beams is a few μK, depending on the eccentricity of the beam response and on the FWHM. Although the $\mathrm{rms_{th}}$ value of this effect may be small compared to the averaged instrumental sensitivity, for some "pixels" the effect may be significantly higher than the average. In addition it cannot be reduced by repeating the observation with different spin axis directions, because (for scanning strategies similar to that proposed by the Planck mission) a given sky region is typically observed with similar orientations of the plane x, y; therefore this kind of distortion produces systematic and not statistical errors in the temperature measurements of any given resolution element.

Deconvolution techniques are generally well established for symmetric beams but it may be difficult to deconvolve observed maps in the case of asymmetric beams, although possible in principle. On the other hand, by averaging maps deconvolved with standard methods and obtained from different channels at the same frequency, this effect, at least in principle, may be reduced, provided that detectors at the same frequency observe the same sky region with different beam orientations. For example, a set of integrations derived from the average of two sets of integrations along the same scan circle and both with the same distortion parameter r but with the major and minor axes of the elliptical response profiles exchanged in the plane x, y for the two cases, presents very small temperature differences with respect to the case of a symmetric beam. We have compared the differences between the temperature observed by a symmetric beam and the average of the temperatures observed by two beams, one like that in the test 2 in Table 1 and the other like that but with the major axis along the y axis: the corresponding value of $\mathrm{rms_{th}}$ is $0.349\,\mu$K, much smaller (by a factor $\sim$6.5) than that obtained in the test 2 and close to the numerical accuracy (see Table 1). Indeed, the average of two elliptical responses with (a) $\sigma_x = \sigma\sqrt{r} > \sigma_y = \sigma/\sqrt{r}$ and (b) $\sigma_x = \sigma/\sqrt{r} < \sigma_y = \sigma\sqrt{r}$ respectively is equal to a symmetric response ($\sigma_x = \sigma_y = \sigma$) multiplied by $1 - 0.25(x^2 + y^2)/\sigma^2(r-1)^2 + ...$, i.e. the first order effect in $(r-1)$ drops out. On the contrary, as already pointed out in the analysis of IRAS data, a simple average of data sets deriving from detectors with significant differences in sensitivity does not allow an analogous improvement. For example, from the temperature differences respect to the observations from a symmetric beam for the simple average of the temperatures obtained in the case (b) with those obtained in the case of a distorted beam like that in the test 1 in Table 1 we have $\mathrm{rms_{th}} = 0.750\,\mu$K, a value very close to that of test 1. On the other hand, by averaging this two data sets with weights inversely proportional to the values of $\mathrm{rms_{th}}$ shown in Table 1 we obtain $\mathrm{rms_{th}} = 0.16\,\mu$K, much smaller (by a factor $\sim$5.2) than that obtained in the test 1 and equal to the numerical accuracy. Analogous improvements cannot be reached by averaging the measurements of beams with distortions oriented in similar direction in the plane x, y. For example, a simple average of the data from test 1 and 2 gives $\mathrm{rms_{th}} = 1.55\,\mu$K; we find only a little improvement from the use of

appropriate weights, obtaining in this case $\mathrm{rms}_{\mathrm{th}} = 1.22\,\mu$K. These results are only intermediate between those of the tests 1 and 2.

These considerations indicate as more advantageous in presence of beam distortions a global feedhorns arrangement in which, for the same frequency, the different beams show distortion figures differently orientated in the plane x, y. Further, an arrangement in which the beams at the same frequency have similar distortion parameters is in general more advantageous respect to an arrangement with a wide spread in the beams distortion parameters; if this is not possible, a careful quantification of the error introduced by the beam distortions is demanded, to correctly average data from beams arrays with wide spreads in optical performances (on the other hand it may be not simply to do it in presence of a large set of systematic effects).

The present analysis shows that, for the same beam distortion parameter r, the effect is more important for the low frequency beams than for high frequency ones, due to the different beam widths. This fact indicates that a good solution may be to arrange low frequency feedhorns near to the optical axis and high frequency ones in the outer regions of the focal plane, because beam distortions typically increase with its distance from the optical axis. On the contrary, when this distance is fixed, the distortion parameter r is typically larger for high frequency detectors than for low frequency ones (Nielsen & Pontoppidan 1996; Villa et al. 1998); this fact suggests a focal plane arrangement that goes in a direction opposite to that delined above. Given the present knowledge of the amount of the beam distortion as a function of the distance from the optical axis and as a function of the frequency and given the present estimate of the distortion effect as a function of the FWHM and of the distortion parameter r, the second choice seems to be more advantageous. On the other hand, the goodness of the focal plane arrangement must be checked by evaluating the average global temperature effect, $\mathrm{rms}_{\mathrm{th}}$, and by minimizing the resulting potential errors introduced by all the distortion effects. An analysis based on preliminary realistic shapes of off-axis beams indicates that elliptical distortions coupled to localized distortions (spots) in the beams responses and to a decreasing in the effective beam angular resolution can produce larger effects on anisotropy measurements, at levels of some μK (Mandolesi et al. 1997, 1998); in these conditions the global effect may be worst than previous estimates and careful simulations for any given optical design are demanded. Another crucial point is the comparison between the $\mathrm{rms}_{\mathrm{th}}$ figures and the sensitivities of the receivers. For Planck LFI, low frequency individual channels are more sensitive (Bersanelli et al. 1996); on the other hand, the 70 and 100 GHz channels are more efficient for the primary cosmological goal.

The full success of missions like Planck and MAP require a good control of all the relevant sources of systematic effects. Discrete sources above the detection limit must be carefully removed and accurate models for foregrounds radiation and anisotropies (Franceschini et al. 1994; De Zotti et al. 1996; Bouchet et al. 1996; Toffolatti et al. 1998) are required to keep the sensitivity degradation in the knowledge of CMB anisotropies below few tens percent (Dodelson 1996). Thermal drifts and stripes generated by the $1/f-$ type noise due to amplifiers gain fluctuations (Janssen et al. 1996; Seiffert et al. 1997) must be minimized by efficient cooling and by optimizing the observational strategy and possibly further reduced in the data analysis (Delabrouille 1998; Burigana et al. 1997).

All in all maximum effort should be addressed to optimize the telescope and the focal plane assembly design in order to minimize the beam distortions effect, one of sources of systematic effects.

Acknowledgements. It is a plesure to thank K. Gorski, E. Hivon, C. Lawrence, M. Malaspina, P. Platania, G. Smoot, L. Toffolatti, F. Villa and M. White for useful discussions and J. Aymon for his exhaustive suggestions on the use of the COBE software. We wish to thank also an anonymous referee for constructive comments.

References

Banday A.J., Wolfendale A.W., 1990, MNRAS 245, 182
Banday A.J., Wolfendale A.W., 1991, MNRAS 248, 705
Bersanelli M., et al., 1996, ESA, COBRAS/SAMBA Report on the Phase A Study, D/SCI(96) 3
Bond J.R., Efstathiou G., 1987, MNRAS 226, 655
Bouchet F.R., et al., 1996, in proceedings of "Microwave Background Anisotropies", XVIth Moriond Astrophysics Meeting, 16-23 March 1996, p. 481
Brandt W.N., et al., 1994, ApJ 424, 1
Burigana C., et al., 1997, in proceedings of Particle Physics and Early Universe Conference, Cambridge 7-11 April 1997, http://www.mrao.cam.ac.uk/ppeuc/proceedings/
Burigana C., Popa, L., 1998, A&A (in press)
Burigana C., et al., 1997, Int. Rep. TeSRE/CNR 198/1997
Danese L., et al., 1996, Astro. Lett. Comm. 33, 257
Delabrouille J., 1998, A&AS 127, 555
De Zotti G., et al., 1996, Astro. Lett. Comm. 35, 289
Dodelson S., 1995, ApJ 482, 577
Franceschini A., et al., 1994, ApJ 427, 140
Gautier T.N., et al., 1992, AJ 103, 1313
Gorski K., 1997, contribution at "CMB Workshop at TAC", Copenhagen, 29-31 May 1997
Janssen M., et al., 1996, astro-ph/9602009
Kogut A., et al., 1996, ApJ 460, 1
Lasenby A., 1997, in proceedings of "Microwave Background Anisotropies", XVIth Moriond Astrophysics Meeting, 16-23 March 1996, p. 453 or astro-ph/9611214

Lawson K.D., et al., 1987, MNRAS 225, 307
Mandolesi N., et al., 1997, Int. Rep. TeSRE/CNR 199/1997
Mandolesi N., et al., 1998 (in preparation)
Muciaccia P.F., et al., 1997, ApJ Lett. 488, L63
Nielsen P.H., Pontoppidan K., 1996, "Design & analysis of the COBRAS/SAMBA telescope", TICRA Rep. S-699-02
Peebles P.J.E., 1980, "The Large-Scale Structure of the Universe". Princeton Univ. Press
Platania P., et al., 1998, ApJ (in press) astro-ph/9707252
Press W.H., et al., 1992, "Numerical Recipes in Fortran". Cambridge University Press
Seiffert M., et al., 1997 (submitted to "The Review of Scientific Instruments")
Toffolatti L., et al., 1995, Astro. Lett. Comm. 32, 125
Toffolatti L., et al., 1998, MNRAS (in press) astro-ph/9711085
Villa F., et al., 1998, Int. Rep. TeSRE/CNR (in preparation)
White M., 1997, contribution at "Planck LFI Consortium Meeting", Tenerife, 2-4 October 1997
White M., et al., 1994, ARA&A 32, 319
Wright E.L., et al., 1991, ApJ 381, 200